



Universiteit Gent  
Faculteit Wetenschappen  
Vakgroep Fysica en Sterrenkunde

2 No title yet

3 No sub-title neither, obviously...

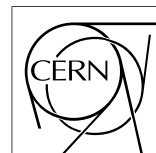
---

4 Alexis Fagot

5



Thesis to obtain the degree of  
Doctor of Philosophy in Physics  
Academic years 2012-2017







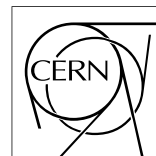
Universiteit Gent  
Faculteit Wetenschappen  
Vakgroep Fysica en Sterrenkunde

7  
8 Promotoren: Dr. Michael Tytgat  
Prof. Dr. Dirk Ryckbosch

9  
10 Universiteit Gent  
11 Faculteit Wetenschappen  
12  
13 Vakgroep Fysica en Sterrenkunde  
14 Proeftuinstraat 86, B-9000 Gent, België  
15 Tel.: +32 9 264.65.28  
16 Fax.: +32 9 264.66.97



Thesis to obtain the degree of  
Doctor of Philosophy in Physics  
Academic years 2012-2017





## Acknowledgements

19 Ici on remerciera tous les gens que j'ai pu croiser durant cette aventure et qui m'ont  
20 permis de passer un bon moment

21 *Gent, ici la super date de la mort qui tue de la fin d'écriture*  
22 *Alexis Fagot*



# Table of Contents

24	<b>Acknowledgements</b>	<b>i</b>
25	<b>Nederlandse samenvatting</b>	<b>xv</b>
26	<b>English summary</b>	<b>xvii</b>
27	<b>1 Introduction</b>	<b>1-1</b>
28	1.1 A story of High Energy Physics . . . . .	1-1
29	1.2 Organisation of this study . . . . .	1-1
30	<b>2 Investigating the TeV scale</b>	<b>2-1</b>
31	2.1 The Standard Model of Particle Physics . . . . .	2-1
32	2.2 The Large Hadron Collider and the Compact Muon Solenoid . . . . .	2-1
33	2.3 Muon Phase-II Upgrade . . . . .	2-1
34	<b>3 Amplification processes in gaseous detectors</b>	<b>3-1</b>
35	3.1 Signal formation . . . . .	3-1
36	3.2 Gas transport parameters . . . . .	3-1
37	<b>4 Resistive Plate Chambers</b>	<b>4-1</b>
38	4.1 Principle . . . . .	4-1
39	4.2 Rate capability of Resistive Plate Chambers . . . . .	4-1
40	4.3 High time resolution . . . . .	4-1
41	4.4 Resistive Plate Chambers at CMS . . . . .	4-1
42	<b>5 Longevity studies and Consolidation of the present CMS RPC subsystem</b>	<b>5-1</b>
43	5.1 Testing detectors under extreme conditions . . . . .	5-3
44	5.1.1 The Gamma Irradiation Facilities . . . . .	5-3
45	5.1.1.1 GIF . . . . .	5-3
46	5.1.1.2 GIF++ . . . . .	5-4
47	5.2 Preliminary tests at GIF . . . . .	5-5
48	5.2.1 Resistive Plate Chamber test setup . . . . .	5-5
49	5.2.2 Data Acquisition . . . . .	5-6
50	5.2.3 Geometrical acceptance of the setup layout to cosmic muons . . . . .	5-8
51	5.2.3.1 Description of the simulation layout . . . . .	5-9
52		

---

53	5.2.3.2	Simulation procedure . . . . .	5-11
54	5.2.3.3	Results . . . . .	5-13
55	5.2.4	Photon flux at GIF . . . . .	5-13
56	5.2.4.1	Expectations from simulations . . . . .	5-13
57	5.2.4.2	Dose measurements . . . . .	5-16
58	5.3	Longevity tests at GIF++ . . . . .	5-17
59	5.3.1	Description of the Data Acquisition . . . . .	5-19
60	5.3.1.1	GIF++ RPC DAQ . . . . .	5-22
61	5.3.1.2	RPC current, environmental and operation pa- rameter monitoring . . . . .	5-23
62	5.3.2	Tools & Measurements . . . . .	5-23
63	5.4	Results and discussions . . . . .	5-23
64	5.4.1	Preliminary studies results . . . . .	5-23
65	5.4.2	Longevity studies results . . . . .	5-23
66			
67	<b>6</b>	<b>Investigation on high rate RPCs</b>	<b>6-1</b>
68	6.1	Rate limitations and ageing of RPCs . . . . .	6-1
69	6.1.1	Low resistivity electrodes . . . . .	6-1
70	6.1.2	Low noise front-end electronics . . . . .	6-1
71	6.2	Construction of prototypes . . . . .	6-1
72	6.3	Results and discussions . . . . .	6-1
73	<b>7</b>	<b>Conclusions and outlooks</b>	<b>7-1</b>
74	7.1	Conclusions . . . . .	7-1
75	7.2	Outlooks . . . . .	7-1
76	<b>A</b>	<b>A data acquisition software for VME CAEN TDCs</b>	<b>A-1</b>
77	A.1	Introduction . . . . .	A-1
78	<b>B</b>	<b>Details on the online analysis package</b>	<b>B-1</b>
79	B.1	Introduction . . . . .	B-1
80	<b>C</b>	<b>Structure of the hybrid simulation software</b>	<b>C-1</b>
81	C.1	Introduction . . . . .	C-1



# List of Figures

83	2.1	Absorbed dose in the CMS cavern after an integrated luminosity	
84		of 3000 fb. R is the transverse distance from the beamline and Z is	
85		the distance along the beamline from the Interaction Point at Z=0.	2-2
86	2.2	A quadrant of the muon system, showing DTs (yellow), RPCs	
87		(light blue), and CSCs (green). The locations of new forward	
88		muon detectors for Phase-II are contained within the dashed box	
89		and indicated in red for GEM stations (ME0, GE1/1, and GE2/1)	
90		and dark blue for improved RPC (iRPC) stations (RE3/1 and RE4/1).	2-3
91	2.3	RMS of the multiple scattering displacement as a function of muon	
92		$p_T$ for the proposed forward muon stations. All of the electromag-	
93		netic processes such as bremsstrahlung and magnetic field effect	
94		are included in the simulation. . . . .	2-3
95	5.1	Figure 5.1a represent the RPC rate measured in 2016 in $p$ - $p$ colli-	
96		sion runs as function of the instantaneous luminosity. Every point	
97		corresponds to a particular run. Figure 5.1b represent the inte-	
98		grated charge for Endcap. The integrated charge in years is shown	
99		in blue. The red curve shows the cumulative evolution of the inte-	
100		grated charge in time. . . . .	5-2
101	5.2	Layout of the test beam zone called X5c GIF at CERN. Photons	
102		from the radioactive source produce a sustained high rate of ran-	
103		dom hits over the whole area. The zone is surrounded by 8 m high	
104		and 80 cm thick concrete walls. Access is possible through three	
105		entry points. Two access doors for personnel and one large gate	
106		for material. A crane allows installation of heavy equipment in the	
107		area. . . . .	5-4
108	5.3	$^{137}\text{Cs}$ decays by $\beta^-$ emission to the ground state of $^{137}\text{Ba}$ (BR =	
109		5.64%) and via the 662 keV isomeric level of $^{137}\text{Ba}$ (BR = 94.36%)	
110		whose half-life is 2.55 min. . . . .	5-4

111	5.4	Description of the RPC setup. Dimensions are given in mm. Figure 5.4a provides a side view of the setup while Figure 5.4b shows a top view. A tent containing RPCs is placed at 1720 mm from the source container. The source is situated in the center of the container. RE-4-2-BARC-161 chamber is 160 mm inside the tent. This way, the distance between the source and the chambers plan is 2060 mm. . . . .	5-5
112			
113			
114			
115			
116			
117			
118	5.5	RE-4-2-BARC-161 chamber is inside the tent as described in Figure 5.4. In the top right, the two scintillators used as trigger can be seen. This trigger system has an inclination of $10^\circ$ relative to horizontal and is placed above half-partition B2 of the RPCs. PMT electronics are shielded thanks to lead blocks placed in order to protect them without stopping photons from going through the scintillators and the chamber. . . . .	5-6
119			
120			
121			
122			
123			
124			
125	5.6	Hit distributions over all 3 partitions of RE-4-2-BARC-161 chamber is showed on these plots. Top, middle and bottom figures respectively correspond to partitions A, B, and C. These plots show that some events still occur in other half-partitions than B2, which corresponds to strips 49 to 64, in front of which the trigger is placed, contributing to the inefficiency of detection of cosmic muons. In the case of partitions A and C, the very low amount of data can be interpreted as noise. On the other hand, it is clear that a little portion of muons reach the half-partition B1, corresponding to strips 33 to 48. . . . .	5-7
126			
127			
128			
129			
130			
131			
132			
133			
134			
135	5.7	Signals from the RPC strips are shaped by the FEE described on Figure 5.7a. Output LVDS signals are then read-out by a TDC module connected to a computer or converted into NIM and sent to scalers. Figure 5.7b describes how these converted signals are put in coincidence with the trigger. . . . .	5-8
136			
137			
138			
139			
140	5.8	Description of the principle of a CFD. A comparison of threshold triggering (left) and constant fraction triggering (right) is shown in Figure 5.8a. Constant fraction triggering is obtained thanks to zero-crossing technique as explained in Figure 5.8b. The signal arriving at the input of the CFD is split into three components. A first one is delayed and connected to the inverting input of a first comparator. A second component is connected to the noninverting input of this first comparator. A third component is connected to the noninverting input of another comparator along with a threshold value connected to the inverting input. Finally, the output of both comparators is fed through an AND gate. . . . .	5-9
141			
142			
143			
144			
145			
146			
147			
148			
149			
150			

151	5.9	Results are derived from data taken on half-partition B2 only. On	
152		the 18 <sup>th</sup> of June 2014, data has been taken on chamber RE-2-	
153		BARC-161 at building 904 (Prevessin Site) with cosmic muons	
154		providing us a reference efficiency plateau of $(97.54 \pm 0.15)\%$ rep-	
155		resented by a black curve. A similar measurement has been done	
156		at GIF on the 21 <sup>st</sup> of July with the same chamber giving a plateau	
157		of $(78.52 \pm 0.94)\%$ represented by a red curve. . . . .	5-10
158	5.10	Representation of the layout used for the simulations of the test	
159		setup. The RPC is represented as a yellow trapezoid while the two	
160		scintillators as blue cuboids looking at the sky. A green plane cor-	
161		responds to the muon generation plane within the simulation. Fig-	
162		ure 5.4a shows a global view of the simulated setup. Figure 5.4b	
163		shows a zoomed view that allows to see the 2 scintillators as well	
164		as the full RPC plane. . . . .	5-11
165	5.11	$\gamma$ flux $F(D)$ is plot using values from table 5.1. As expected, the	
166		plot shows similar attenuation behaviours with increasing distance	
167		for each absorption factors. . . . .	5-14
168	5.12	Figure 5.12a shows the linear approximation fit done via formul-	
169		ae 5.7 on data from table 5.2. Figure 5.12b shows a comparison	
170		of this model with the simulated flux using a and b given in fig-	
171		ure 5.12a in formulae 5.4 and the reference value $D_0 = 50cm$	
172		and the associated flux for each absorption factor $F_0^{ABS}$ from ta-	
173		ble 5.1 . . . . .	5-16
174	5.13	Dose measurements has been done in a plane corresponding to the	
175		tents front side. This plan is 1900 mm away from the source. As	
176		explained in the first chapter, a lens-shaped lead filter provides a	
177		uniform photon flux in the vertical plan orthogonal to the beam	
178		direction. If the second line of measured fluxes is not taken into	
179		account because of lower values due to experimental equipments	
180		in the way between the source and the tent, the uniformity of the	
181		flux is well showed by the results. . . . .	5-17
182	5.14	Evolution of the maximum efficiency for RE2 (5.14a) and RE4	
183		(5.14b) chambers with increasing extrapolated $\gamma$ rate per unit area	
184		at working point. Both irradiated (blue) and non irradiated (red)	
185		chambers are shown. . . . .	5-19
186	5.15	Evolution of the working point for RE2 (5.15a) and RE4 (5.15b)	
187		with increasing extrapolated $\gamma$ rate per unit area at working point.	
188		Both irradiated (blue) and non irradiated (red) chambers are shown.	5-19
189	5.16	Evolution of the maximum efficiency at HL-LHC conditions, i.e.	
190		a background hit rate per unit area of $300 \text{ Hz/cm}^2$ , with increasing	
191		integrated charge for RE2 (5.16a) and RE4 (5.16b) detectors. Both	
192		irradiated (blue) and non irradiated (red) chambers are shown. The	
193		integrated charge for non irradiated detectors is recorded during	
194		test beam periods and stays small with respect to the charge accu-	
195		culated in irradiated chambers. . . . .	5-20

196	5.17	Comparison of the efficiency sigmoid before (triangles) and after	
197		(circles) irradiation for RE2 (5.17a) and RE4 (5.17b) detectors.	
198		Both irradiated (blue) and non irradiated (red) chambers are shown.	5-20
199	5.18	Evolution of the Bakelite resistivity for RE2 (5.18a) and RE4 (5.18b)	
200		detectors. Both irradiated (blue) and non irradiated (red) chambers	
201		are shown. . . . .	5-21
202	5.19	Evolution of the noise rate per unit area for the irradiated chamber	
203		RE2-2-BARC-9 only. . . . .	5-21
204	5.20	. . . . .	5-24

## List of Tables

206	5.1	Total photon flux ( $E\gamma \leq 662 \text{ keV}$ ) with statistical error predicted	
207		considering a $^{137}\text{Cs}$ activity of 740 GBq at different values of the	
208		distance $D$ to the source along the x-axis of irradiation field [6]. .	5-13
209	5.2	Correction factor $c$ is computed thanks to formulae 5.5 taking as	
210		reference $D_0 = 50 \text{ cm}$ and the associated flux $F_0^{ABS}$ for each ab-	
211		sorption factor available in table 5.1. . . . .	5-15
212	5.3	The data at $D_0$ in 1997 is taken from [6]. In a second step, using	
213		Equations 5.8 and 5.9, the flux at $D$ can be estimated in 1997.	
214		Then, taking into account the attenuation of the source activity,	
215		the flux at $D$ can be estimated at the time of the tests in GIF in	
216		2014. Finally, assuming a sensitivity of the RPC to $\gamma s = 2 \cdot 10^{-3}$ ,	
217		an estimation of the hit rate per unit area is obtained. . . . .	5-17



218

# List of Acronyms

219

## List of Acronyms

220

221

222

### B

223

224 BARC  
225 BR

Bhabha Atomic Research Centre  
Branching Ratio

226

227

228

### C

229

230 CAEN  
231

Costruzioni Apparecchiature Elettroniche Nucleari S.p.A.

232 CERN  
233 CFD

European Organization for Nuclear Research  
Constant Fraction Discriminator

234 CMS  
235 CSC

Compact Muon Solenoid  
Cathode Strip Chamber

236

237

238

### D

239

240 DAQ  
241 DCS  
242 DQM  
243 DT

Data Acquisition  
Detector Control Software  
Data Quality Monitoring  
Drift Tube

244

245

246

### F

247

248 FEE

Front-End Electronics

249	FEB	Front-End Board
250		
251		
252	<b>G</b>	
253		
254	GE-/-	Find a good description
255	GE1/1	Find a good description
256	GE2/1	Find a good description
257	GEANT	GEometry ANd Tracking - a series of software toolkit platforms developed by CERN
258		
259	GEM	Gas Electron Multiplier
260	GIF	old Gamma Irradiation Facility dismantled in 2014
261	GIF++	new Gamma Irradiation Facility
262		
263		
264	<b>H</b>	
265		
266	HL-LHC	High Luminosity LHC
267	HV	High Voltage
268		
269		
270	<b>I</b>	
271		
272	iRPC	improved RPC
273		
274		
275	<b>L</b>	
276		
277	LHC	Large Hadron Collider
278	LS1	First Long Shutdown
279	LS3	Third Long Shutdown
280	LV	Low Voltage
281	LVDS	Low-Voltage Differential Signaling
282		
283		
284	<b>M</b>	
285		
286	MC	Monte Carlo



---

287	MCNP	Monte Carlo N-Particle
288	ME-/-	Find good description
289	ME0	Find good description
290		
291		
292	<b>N</b>	
293		
294	NIM	Nuclear Instrumentation Module logic signals
295		
296		
297	<b>P</b>	
298		
299	PMT	PhotoMultiplier Tube
300		
301		
302	<b>R</b>	
303		
304	RE-/-	Find a good description
305	RE2/2	Find a good description
306	RE3/1	Find a good description
307	RE3/2	Find a good description
308	RE4/1	Find a good description
309	RE4/2	Find a good description
310	RE4/3	Find a good description
311	RMS	Root Mean Square
312	ROOT	a framework for data processing born at CERN
313	RPC	Resistive Plate Chamber
314		
315		
316	<b>S</b>	
317		
318	SPS	Super Proton Synchrotron
319		
320		
321	<b>T</b>	
322		
323	TDC	Time-to-Digital Converter



325

## Nederlandse samenvatting –Summary in Dutch–

326

327 Le resume en Neerlandais (j'aurais peut-etre de apprendre la langue juste pour  
328 ca...).



## English summary

330 Le meme résumé mais en Anglais (on commencera par la hein!).



# 1

## Introduction

331

332

333 **1.1 A story of High Energy Physics**

334 **1.2 Organisation of this study**





# 2

## Investigating the TeV scale

### 2.1 The Standard Model of Particle Physics

### 2.2 The Large Hadron Collider and the Compact Muon Solenoid

### 2.3 Muon Phase-II Upgrade

After the more than two years lasting First Long Shutdown (LS1), the Large Hadron Collider (LHC) delivered its very first Run-II proton-proton collisions early 2015. LS1 gave the opportunity to the LHC and to the its experiments to undergo upgrades. The accelerator is now providing collisions at center-of-mass energy of 13 TeV and bunch crossing rate of 40 MHz, with a peak luminosity exceeding its design value. During the first and upcoming second LHC Long Shutdown, the Compact Muon Solenoid (CMS) detector is also undergoing a number of upgrades to maintain a high system performance [1].

From the LHC Phase-2 or High Luminosity LHC (HL-LHC) period onwards, i.e. past the Third Long Shutdown (LS3), the performance degradation due to integrated radiation as well as the average number of inelastic collisions per bunch crossing, or pileup, will rise substantially and become a major challenge for the LHC experiments, like CMS that are forced to address an upgrade program for Phase-II [2]. Simulations of the expected distribution of absorbed dose in the CMS detector under HL-LHC conditions, show in figure 5.13 that detectors placed close

to the beamline will have to withstand high irradiation, the radiation dose being of the order of a few tens of Gy.

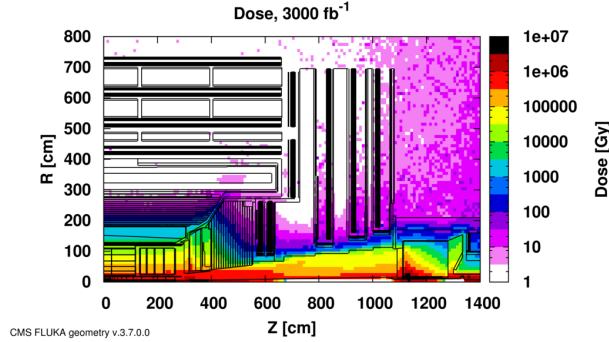


Figure 2.1: Absorbed dose in the CMS cavern after an integrated luminosity of 3000 fb.  $R$  is the transverse distance from the beamline and  $Z$  is the distance along the beamline from the Interaction Point at  $Z=0$ .

The measurement of small production cross-section and/or decay branching ratio processes, such as the Higgs boson coupling to charge leptons or the  $B_s \rightarrow \mu^+ \mu^-$  decay, is of major interest and specific upgrades in the forward regions of the detector will be required to maximize the physics acceptance on the largest possible solid angle. To ensure proper trigger performance within the present coverage, the muon system will be completed with new chambers. In figure 2.2 one can see that the existing Cathode Strip Chambers (CSCs) will be completed by Gas Electron Multipliers (GEMs) and Resistive Plate Chambers (RPCs) in the pseudorapidity region  $1.6 < |\eta| < 2.4$  to complete its redundancy as originally scheduled in the CMS Technical Proposal [3].

RPCs are used by the CMS first level trigger for their good timing performances. Indeed, a very good bunch crossing identification can be obtained with the present CMS RPC system, given their fast response of the order of 1 ns. In order to contribute to the precision of muon momentum measurements, muon chambers should have a spatial resolution less or comparable to the contribution of multiple scattering [1]. Most of the plausible physics is covered only considering muons with  $p_T < 100$  GeV thus, in order to match CMS requirements, a spatial resolution of  $\mathcal{O}(\text{few mm})$  the proposed new RPC stations, as shown by the simulation in figure 2.3. According to preliminary designs, RE3/1 and RE4/1 readout pitch will be comprised between 3 and 6 mm and 5  $\eta$ -partitions could be considered.

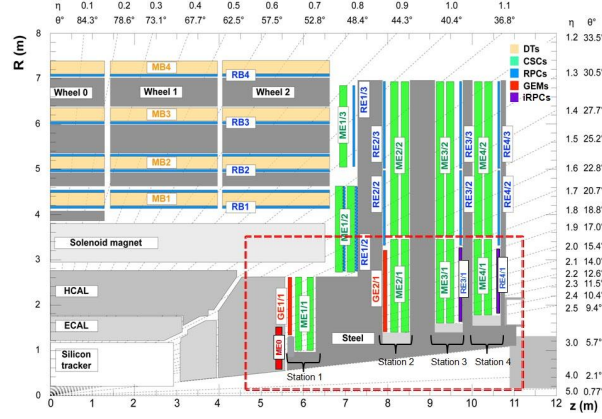


Figure 2.2: A quadrant of the muon system, showing DTs (yellow), RPCs (light blue), and CSCs (green). The locations of new forward muon detectors for Phase-II are contained within the dashed box and indicated in red for GEM stations (ME0, GE1/1, and GE2/1) and dark blue for improved RPC (iRPC) stations (RE3/1 and RE4/1).

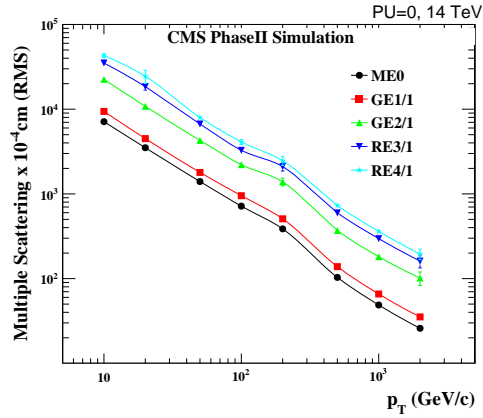


Figure 2.3: RMS of the multiple scattering displacement as a function of muon  $p_T$  for the proposed forward muon stations. All of the electromagnetic processes such as bremsstrahlung and magnetic field effect are included in the simulation.



# 3

378

379

## Amplification processes in gaseous detectors

380

381 **3.1 Signal formation**

382 **3.2 Gas transport parameters**



# 4

383

384

## Resistive Plate Chambers

385 **4.1 Principle**

386 **4.2 Rate capability of Resistive Plate Chambers**

387 **4.3 High time resolution**

388 **4.4 Resistive Plate Chambers at CMS**





# 5

389

## 390 Longevity studies and Consolidation of 391 the present CMS RPC subsystem

392 The upgrade from LHC to HL-LHC will increase the peak luminosity from  $10^{34}$   
393  $\text{cm}^{-2} \text{s}^{-1}$  to reach  $7.5 \times 10^{34} \text{cm}^{-2} \text{s}^{-1}$ , increasing in the same way the total ex-  
394 pected background to which the RPC system will be subjected to. Composed of  
395 low energy gammas and neutrons from  $p$ - $p$  collisions, low momentum primary  
396 and secondary muons, punch-through hadrons from calorimeters, and particles pro-  
397 duced in the interaction of the beams with collimators, the background will mostly  
398 affect the regions of CMS that are the closest to the beam line, i.e. the RPC detec-  
399 tors located in the endcaps.

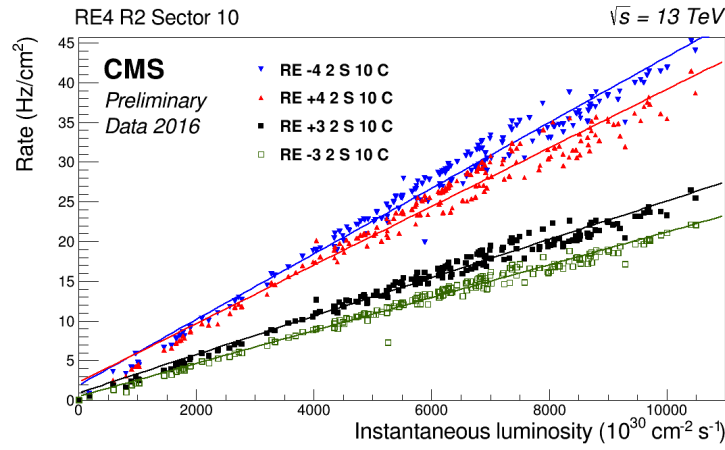
400

401 The information collected with 2016 data allowed us to understand that the  
402 hottest RPC regions are located in the fourth endcap stations. Extrapolating from  
403 the data shown in Figure 5.1, the maximum rate per unit area under HL-LHC con-  
404 ditions is therefore foreseen to increase to values of the order of  $400 \text{ Hz/cm}^2$  in the  
405 chambers of the present muon system. To the  $4000 \text{ fb}^{-1}$  of integrated luminosity,  
406 over the 10 years of HL-LHC lifetime, will correspond  $\sim 0.4 \text{ C/cm}^2$  of integrated  
407 charge inside the hottest regions of the detectors, considering the current total de-  
408 livered luminosity from  $p$ - $p$  collisions of about  $75 \text{ fb}^{-1}$  and the total integrated  
409 charge estimated to be about  $5.8 \text{ mC/cm}^2$  in the endcap.

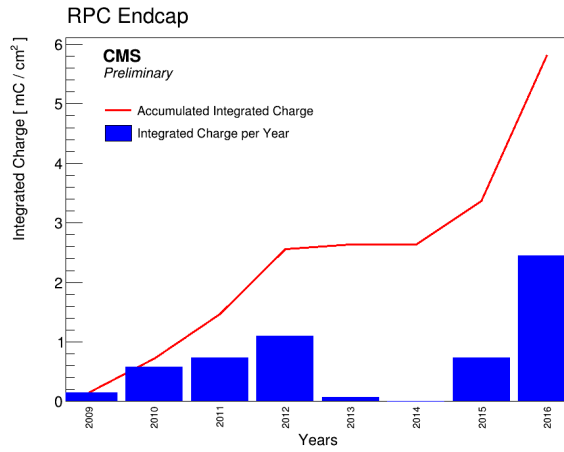
410

411 During Run-I, the RPC system provided stable operation and excellent per-  
412 formance and did not show any aging effects. In the past, extensive long-term

tests were carried out at several gamma and neutron facilities certifying the detector performance up to values of dose, charge and fluence close to those expected after ten years of HL-LHC operation. Both full size and small prototype RPCs have been irradiated with photons up to an integrated charge of  $\sim 0.05 \text{ C/cm}^2$  and  $\sim 0.4 \text{ C/cm}^2$ , respectively [4, 5].



(a)



(b)

Figure 5.1: Figure 5.1a represent the RPC rate measured in 2016 in  $p$ - $p$  collision runs as function of the instantaneous luminosity. Every point corresponds to a particular run. Figure 5.1b represent the integrated charge for Endcap. The integrated charge in years is shown in blue. The red curve shows the cumulative evolution of the integrated charge in time.

In this perspective, studying the performance of the present system up to an integrated charge of  $\sim 1.2 \text{ C/cm}^2$ , 3 times higher than what expected for 10 years of operation of HL-LHC, and background hit rates of  $1200 \text{ Hz/cm}^2$ , 3 times stronger than what expected from the designed peak luminosity, and identifying possible long-term aging effects are necessary steps to take to insure that the RPCs will be able to cope with the high radiation conditions.

## 5.1 Testing detectors under extreme conditions

### 5.1.1 The Gamma Irradiation Facilities

#### 5.1.1.1 GIF

Located in the SPS West Area at the downstream end of the X5 test beam, GIF was a test area in which particle detectors were exposed to a particle beam in presence of an adjustable gamma background [6]. Its goal was to reproduce background conditions these detectors would suffer in their operating environment at LHC. GIF layout is shown in Figure 5.2. Gamma photons are produced by a strong  $^{137}\text{Cs}$  source installed in the upstream part of the zone inside a lead container. The source container includes a collimator, designed to irradiate a  $6 \times 6 \text{ m}^2$  area at 5 m maximum to the source. A thin lens-shaped lead filter helps providing with a uniform outcoming flux in a vertical plane, orthogonal to the beam direction. The principal collimator hole provides a pyramidal aperture of  $74^\circ \times 74^\circ$  solid angle and provides a photon flux in a pyramidal volume along the beam axis. The photon rate is controlled by further lead filters allowing the maximum rate to be limited and to vary within a range of four orders of magnitude. Particle detectors under test are then placed within the pyramidal volume in front of the source, perpendicularly to the beam line in order to profit from the homogeneous photon flux. Adjusting the background flux of photons can then be done by using the filters and choosing the position of the detectors with respect to the source.

As described on Figure 5.3, the  $^{137}\text{Cs}$  source emits a 662 keV photon in 85% of the decays. An activity of 740 GBq was measured on the 5<sup>th</sup> March 1997. To estimate the strength of the flux in 2014, it is necessary to consider the nuclear decay through time associated to the Cesium source whose half-life is well known ( $t_{1/2} = (30.05 \pm 0.08) \text{ y}$ ). The GIF tests were done in between the 20<sup>th</sup> and the 31<sup>st</sup> of August 2014, i.e. at a time  $t = (17.47 \pm 0.02) \text{ y}$  resulting in an attenuation of the activity from 740 GBq in 1997 to 494 GBq in 2014.

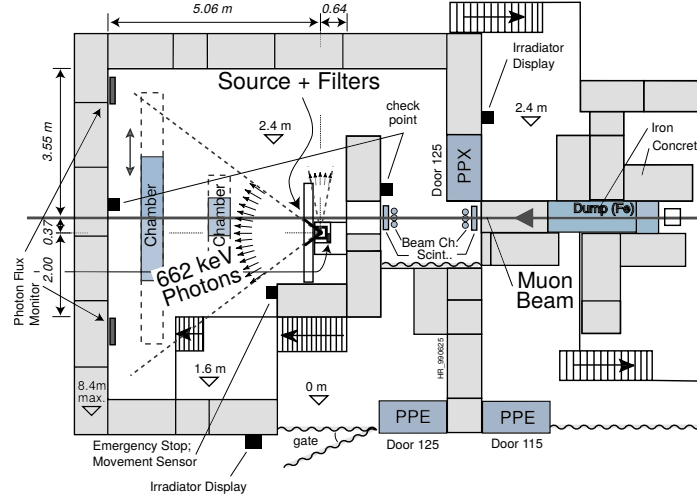


Figure 5.2: Layout of the test beam zone called X5c GIF at CERN. Photons from the radioactive source produce a sustained high rate of random hits over the whole area. The zone is surrounded by 8 m high and 80 cm thick concrete walls. Access is possible through three entry points. Two access doors for personnel and one large gate for material. A crane allows installation of heavy equipment in the area.

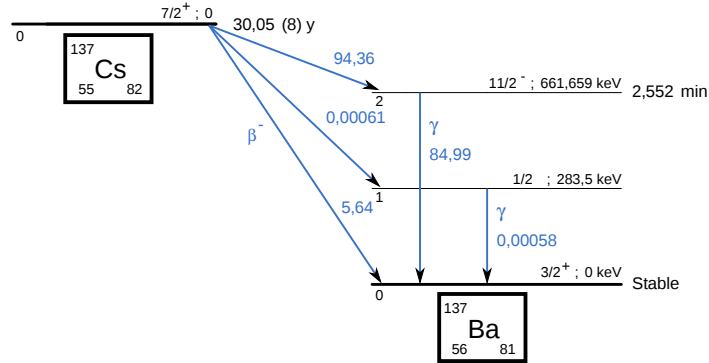


Figure 5.3:  $^{137}\text{Cs}$  decays by  $\beta^-$  emission to the ground state of  $^{137}\text{Ba}$  (BR = 5.64%) and via the 662 keV isomeric level of  $^{137}\text{Ba}$  (BR = 94.36%) whose half-life is 2.55 min.

#### 5.1.1.2 GIF++

GIF++ is a test area located in the SPS North Area at the downstream end of the H4 test beam. In this facility, particle detectors are tested using a particle beam in presence of an adjustable background flux of photons. The goal is to

459 simulate background conditions these detectors would suffer in their operating  
 460 environment at the HL-LHC. Gamma photons are produced by a strong radioactive  
 461  $^{137}\text{Cs}$  source installed in the center part of the zone, with an activity of 13.1 TBq,  
 462 emitting 662 keV photons. A thin lens-shaped lead filter renders the outcoming  
 463 flux uniform in the vertical plane orthogonal to the beam direction. Control of the  
 464 photon rate is achieved by using a set of filters allowing the maximum rate to be  
 465 limited and to vary within a range of four orders of magnitude. The H4 beam,  
 466 composed of muons with a momentum of about 150 GeV/c, passes through the  
 467 GIF++ zone and is used to study the performance of the detectors. Its flux is of  
 468  $104 \text{ particles/s/cm}^2$  focused in an area similar to  $10 \times 10 \text{ cm}^2$ .

## 469 5.2 Preliminary tests at GIF

### 470 5.2.1 Resistive Plate Chamber test setup

471 During summer 2014, preliminary tests have been conducted in the GIF area on  
 472 a newly produced RE4/2 chamber labelled RE-4-2-BARC-161. This chamber has  
 473 been placed into a trolley covered with a tent. The position of the RPC inside the  
 474 tent and of the tent related to the source is described in Figure 5.4. To test this  
 475 CMS RPC, three different absorber settings were used. First of all, measurements  
 476 were done with fully opened source. Then, to complete this preliminary study, the  
 477 gamma flux has been attenuated by a factor 2 and a factor 5. The expected gamma  
 478 flux at the level of our detector will be discussed in subsection 5.2.4.

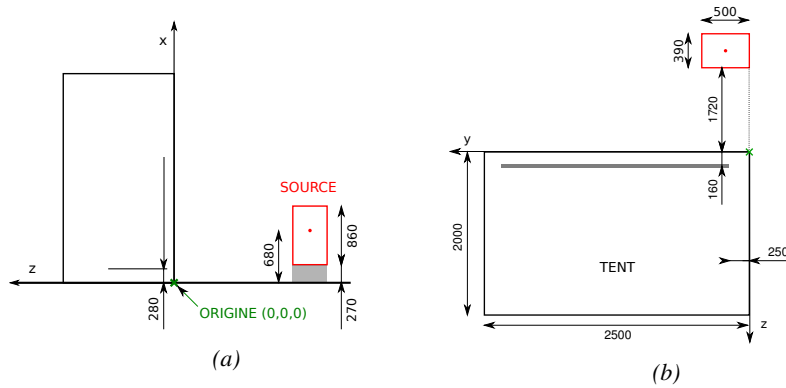


Figure 5.4: Description of the RPC setup. Dimensions are given in mm. Figure 5.4a provides a side view of the setup while Figure 5.4b shows a top view. A tent containing RPCs is placed at 1720 mm from the source container. The source is situated in the center of the container. RE-4-2-BARC-161 chamber is 160 mm inside the tent. This way, the distance between the source and the chambers plan is 2060 mm.

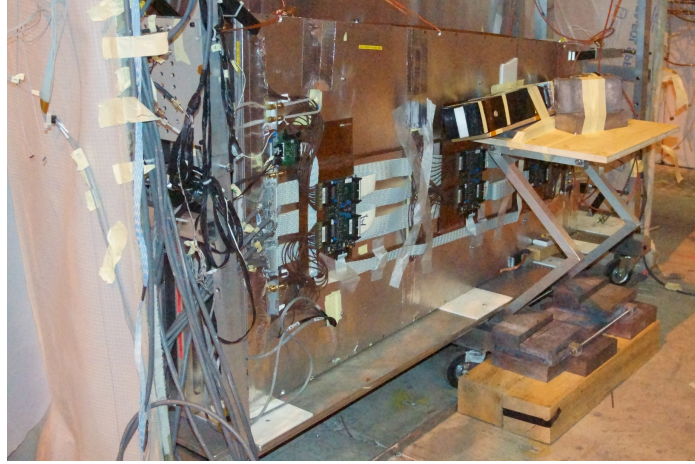


Figure 5.5: RE-4-2-BARC-161 chamber is inside the tent as described in Figure 5.4. In the top right, the two scintillators used as trigger can be seen. This trigger system has an inclination of  $10^\circ$  relative to horizontal and is placed above half-partition B2 of the RPCs. PMT electronics are shielded thanks to lead blocks placed in order to protect them without stopping photons from going through the scintillators and the chamber.

At the time of the tests, the beam not being operationnal anymore, a trigger composed of 2 plastic scintillators has been placed in front of the setup with an inclination of 10 deg (*this has to be first confirmed by the simulation - I will adjust in consequence cause it has never been precisely measured*) with respect to the detector plane in order to look at cosmic muons. Using this particular trigger layout, shown on Figure 5.5, leads to a cosmic muon hit distribution into the chamber similar to the one in Figure 5.6. Measured without gamma irradiation, two peaks can be seen on the profil of partition B, centered on strips 52 and 59. Sub-section 5.2.3 will help us understand that these two peaks are due respectively to forward and backward coming cosmic particles where forward coming particles are first detected by the scintillators and then the RPC while the backward coming muons are first detected in the RPC.

## 5.2.2 Data Acquisition

Signals induced by cosmic particle in the RPC strips are shaped by standard CMS RPC Front-End Electronics (FEE) following the scheme of Figure 5.7. On a first stage, analogic signals are amplified and then sent to the Constant Fraction Discriminator (CFD) described in Figure 5.8. At the end of the chain, 100 ns long pulses are sent in the LVDS output. These output signal are sent on one side to a V1190A Time-to-Digital Converter (TDC) module from CAEN and on the other

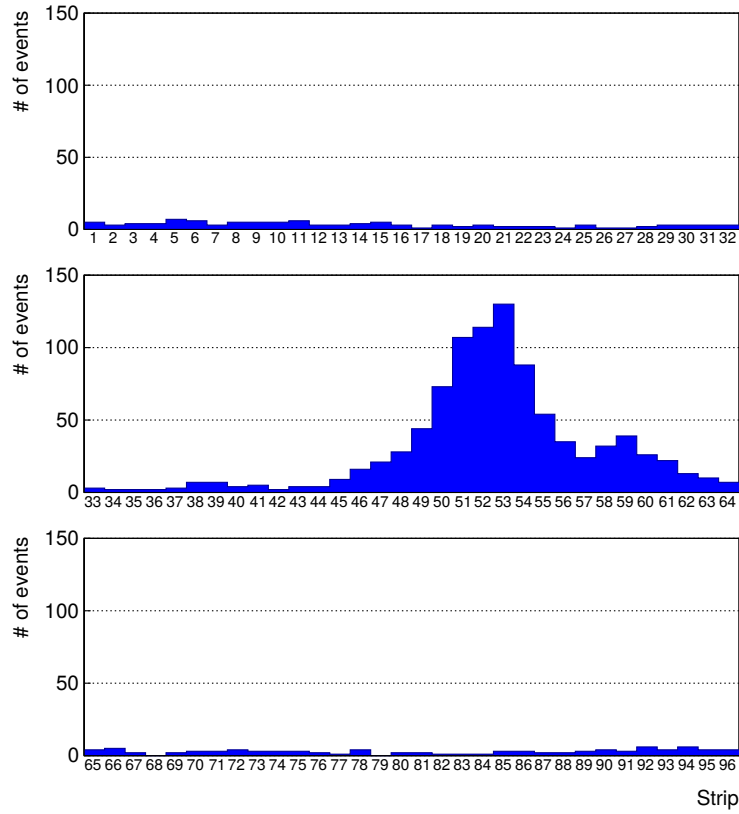


Figure 5.6: Hit distributions over all 3 partitions of RE-4-2-BARC-161 chamber is showed on these plots. Top, middle and bottom figures respectively correspond to partitions A, B, and C. These plots show that some events still occur in other half-partitions than B2, which corresponds to strips 49 to 64, in front of which the trigger is placed, contributing to the inefficiency of detection of cosmic muons. In the case of partitions A and C, the very low amount of data can be interpreted as noise. On the other hand, it is clear that a little portion of muons reach the half-partition B1, corresponding to strips 33 to 48.

498 to an OR module to count the number of detected signals. Trigger and hit coïnci-  
 499 dences are monitored using scalers. The TDC is used to store the data into ROOT  
 500 files. These files are thus analysed to understand the detectors performance.

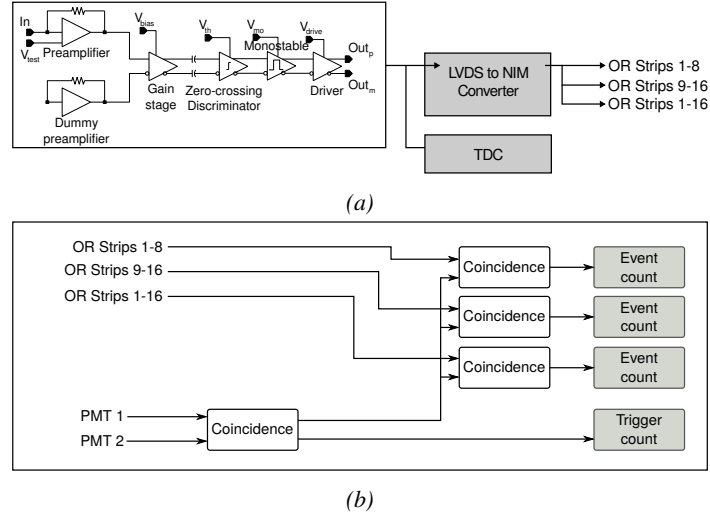


Figure 5.7: Signals from the RPC strips are shaped by the FEE described on Figure 5.7a. Output LVDS signals are then read-out by a TDC module connected to a computer or converted into NIM and sent to scalers. Figure 5.7b describes how these converted signals are put in coincidence with the trigger.

### 5.2.3 Geometrical acceptance of the setup layout to cosmic muons

In order to profit from a constant gamma irradiation, the detectors inside of the GIF bunker need to be placed in a plane orthogonal to the beam line. The muon beam that used to be available was meant to test the performance of detectors under test. This beam not being active anymore, another solution to test detector performance had to be used. Thus, it has been decided to use cosmic muons detected through a telescope composed of two scintillators. Lead blocks were used as shielding to protect the photomultipliers from gammas as can be seen from Figure 5.5.

An inclination has been given to the cosmic telescope to maximize the muon flux. A good compromise had to be found between good enough muon flux and narrow enough hit distribution to be sure to contain all the events into only one half partitions as required from the limited available readout hardware. Nevertheless, a consequence of the misplaced trigger, that can be seen as a loss of events in half-partition B1 in Figure 5.6, is an inefficiency. Nevertheless, the inefficiency of approximately 20 % highlighted in Figure 5.9 by comparing the performance of chamber BARC-161 in 904 and at GIF without irradiation seems too important to be explained only by the geometrical acceptance of the setup itself. Simulations have been conducted to show how the setup brings inefficiency.



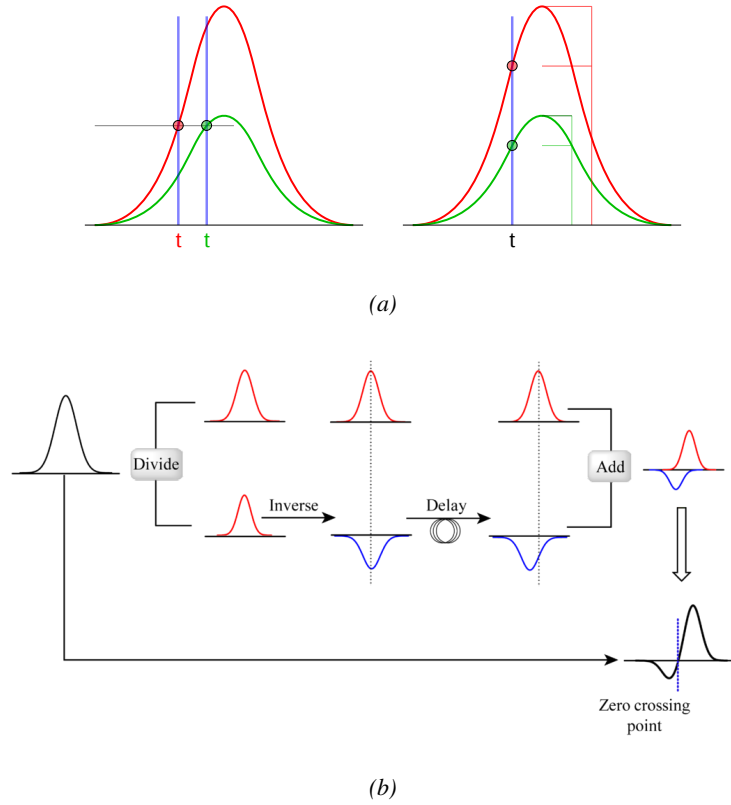


Figure 5.8: Description of the principle of a CFD. A comparison of threshold triggering (left) and constant fraction triggering (right) is shown in Figure 5.8a. Constant fraction triggering is obtained thanks to zero-crossing technique as explained in Figure 5.8b. The signal arriving at the input of the CFD is split into three components. A first one is delayed and connected to the inverting input of a first comparator. A second component is connected to the noninverting input of this first comparator. A third component is connected to the noninverting input of another comparator along with a threshold value connected to the inverting input. Finally, the output of both comparators is fed through an AND gate.

### 5.2.3.1 Description of the simulation layout

The layout of GIF setup has been reproduced and incorporated into a Monte Carlo (MC) simulation to study the influence of the disposition of the telescope on the final distribution measured by the RPC. A 3D view of the simulated layout is given into Figure 5.10. Muons are generated randomly in a horizontal plane located at a height corresponding to the lowest point of the PMTs. This way, the needed size of the plane in order to simulate events happening at very big azimuthal angles (i.e.  $\theta \approx \pi$ ) can be kept relatively small. The muon flux is designed to follow the usual

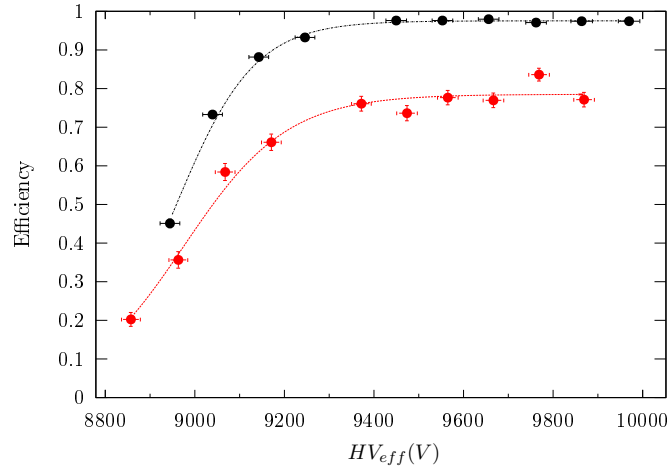


Figure 5.9: Results are derived from data taken on half-partition B2 only. On the 18<sup>th</sup> of June 2014, data has been taken on chamber RE-2-BARC-161 at building 904 (Preveessin Site) with cosmic muons providing us a reference efficiency plateau of  $(97.54 \pm 0.15)\%$  represented by a black curve. A similar measurement has been done at GIF on the 21<sup>st</sup> of July with the same chamber giving a plateau of  $(78.52 \pm 0.94)\%$  represented by a red curve.

527  $\cos^2\theta$  distribution for cosmic particle. The goal of the simulation is to look at  
 528 muons that pass through the muon telescope composed of the two scintillators and  
 529 define their distribution onto the RPC plane. During the reconstruction, the RPC  
 530 plane is then divided into its strips and each muon track is assigned to a strip.

531 In order to further refine the quality of the simulation and understand deeper  
 532 the results the dependance of the distribution has been studied for a range of tele-  
 533 scope inclinations. Moreover, the threshold applied on the PMT signals has been  
 534 included into the simulation in the form of a cut. In the approximation of uni-  
 535 form scintillators, it has been considered that the threshold can be understood as  
 536 the minimum distance particles need to travel through the scintillating material to  
 537 give a strong enough signal. Particles that travel a distance smaller than the set  
 538 "threshold" are thus not detected by the telescope and cannot trigger the data tak-  
 539 ing. Finally, the FEE threshold also has been considered in a similar way. The  
 540 mean momentum of horizontal cosmic rays is higher than those of vertical ones  
 541 but the stopping power of matter for momenta ranging from 1 GeV to 1 TeV stays  
 542 comparable. It is then possible to assume that the mean number of primary  $e^-$ /ion  
 543 pairs per unit length will stay similar and thus, depending on the applied discrimi-  
 544 nator threshold, muons with the shortest path through the gas volume will deposit  
 545 less charge and induce a smaller signal on the pick-up strips that could eventu-

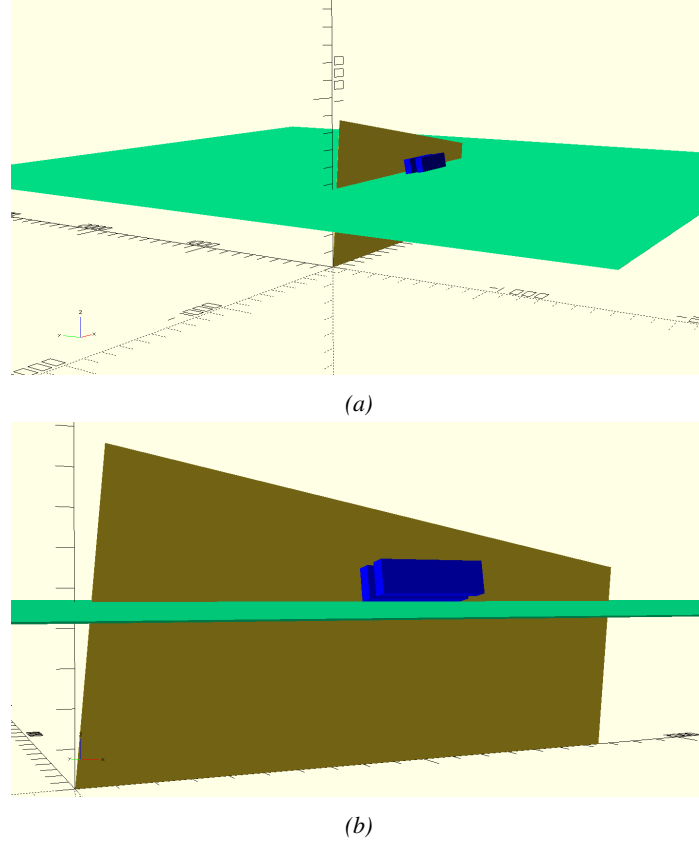


Figure 5.10: Representation of the layout used for the simulations of the test setup. The RPC is represented as a yellow trapezoid while the two scintillators as blue cuboids looking at the sky. A green plane corresponds to the muon generation plane within the simulation. Figure 5.4a shows a global view of the simulated setup. Figure 5.4b shows a zoomed view that allows to see the 2 scintillators as well as the full RPC plane.

ally not be detected. These two thresholds also restrain the overall geometrical acceptance of the system.

### 5.2.3.2 Simulation procedure

The simulation software has been designed using C++ and the output data is saved into ROOT histograms. Simulations start for a threshold  $T_{scint}$  varying in a range from 0 to 45 mm in steps of 5 mm, where  $T_{scint} = 0$  mm corresponds to the case where there isn't any threshold apply on the input signal while  $T_{scint} = 45$  mm, which is the scintillator thickness, is the case where muons cannot arrive orthogonally onto the scintillator surface. For a given  $T_{scint}$ , a set of RPC thresholds are

considered. The RPC threshold,  $T_{RPC}$  varies from 2 mm, the thickness of the gas volume, to 3 mm in steps of 0.25 mm. For each  $(T_{scint}; T_{RPC})$  pair,  $N_\mu = 10^8$  muons are randomly generated inside the muon plane described in the previous paragraph with an azimuthal angle  $\theta$  chosen to follow a  $\cos^2\theta$  distribution.

Planes are associated to each surface of the scintillators. Knowing muon position into the muon plane and its direction allows us, by assuming that muons travel in a straight line, to compute the intersection of the muon track with these planes. Applying conditions to the limits of the surfaces of the scintillator faces then gives us an answer to whether or not the muon passed through the scintillators. In the case the muon has indeed passed through the telescope, the path through each scintillator is computed and muons whose path was shorter than  $T_{scint}$  are rejected and are thus considered as having not interacted with the setup.

On the contrary, if the muon is labeled as good, its position within the RPC plane is computed and the corresponding strip, determined by geometrical tests in the case the distance through the gas volume was enough not to be rejected because of  $T_{RPC}$ , gets a hit and several histograms are filled in order to keep track of the generation point on the muon plane, the intersection points of the reconstructed muons within the telescope, or on the RPC plane, the path traveled through each individual scintillator or the gas volume, as well as other histograms. Moreover, muons fill different histograms whether they are forward or backward coming muons. They are discriminated according to their direction components. When a muon is generated, an  $(x, y, z)$  position is assigned into the muon plane as well as a  $(\theta; \phi)$  pair that gives us the direction it's coming from. This way, muons satisfying the condition  $0 \leq \phi < \pi$  are designated as backward coming muons while muons satisfying  $\pi \leq \phi < 2\pi$  as forward coming muons.

This simulation is then repeated for different telescope inclinations ranging in between 4 and 20° and varying in steps of 2°. Due to this inclination and to the vertical position of the detector under test, the muon distribution reconstructed in the detector plane is asymmetrical. The choice has been made to choose a skew distribution formula to fit the data built as the multiplication of gaussian and sigmoidal curves together. A typical gaussian formula is given as 5.1 and has three free parameters as  $A_g$ , its amplitude,  $\bar{x}$ , its mean value and  $\sigma$ , its root mean square. Sigmoidal curves as given by formula 5.2 are functions converging to 0 and  $A_s$  as  $x$  diverges. The inflexion point is given as  $x_i$  and  $\lambda$  is proportional to the slope at  $x = x_i$ . In the limit where  $\lambda \rightarrow \infty$ , the sigmoid becomes a step function.

$$g(x) = A_g e^{\frac{-(x-\bar{x})^2}{2\sigma^2}} \quad (5.1)$$

$$s(x) = \frac{A_s}{1 + e^{-\lambda(x-x_i)}} \quad (5.2)$$

590 Finally, a possible representation of a skew distribution is given by formula 5.3  
 591 and is the product of 5.1 and 5.2. Naturally, here  $A_{sk} = A_g \times A_s$  and represents  
 592 the theoretical maximum in the limit where the skew tends to a gaussian function.

$$sk(x) = g(x) \times s(x) = A_{sk} \frac{e^{-\frac{(x-\bar{x})^2}{2\sigma^2}}}{1 + e^{-\lambda(x-x_i)}} \quad (5.3)$$

### 593 5.2.3.3 Results

594 **Influence of  $T_{scint}$  on the muon distribution**

595 **Influence of  $T_{RPC}$  on the muon distribution**

596 **Influence of the telescope inclination on the muon distribution**

597 **Comparison to data taken at GIF without irradiation**

## 598 5.2.4 Photon flux at GIF

### 599 5.2.4.1 Expectations from simulations

600 In order to understand and evaluate the  $\gamma$  flux in the GIF area, simulations had been  
 601 conducted in 1999 and published by S. Agosteo et al [6]. Table 5.1 presented in  
 602 this article gives us the  $\gamma$  flux for different distances  $D$  to the source. This sim-  
 603 ulation was done using GEANT and a Monte Carlo N-Particle (MCNP) transport  
 604 code, and the flux  $F$  is given in number of  $\gamma$  per unit area and unit time along with  
 605 the estimated error from these packages expressed in %.

Nominal ABS	Photon flux $F$ [ $s^{-1}cm^{-2}$ ]			
	at $D = 50$ cm	at $D = 155$ cm	at $D = 300$ cm	at $D = 400$ cm
1	$0.12 \cdot 10^8 \pm 0.2\%$	$0.14 \cdot 10^7 \pm 0.5\%$	$0.45 \cdot 10^6 \pm 0.5\%$	$0.28 \cdot 10^6 \pm 0.5\%$
2	$0.68 \cdot 10^7 \pm 0.3\%$	$0.80 \cdot 10^6 \pm 0.8\%$	$0.25 \cdot 10^6 \pm 0.8\%$	$0.16 \cdot 10^6 \pm 0.6\%$
5	$0.31 \cdot 10^7 \pm 0.4\%$	$0.36 \cdot 10^6 \pm 1.2\%$	$0.11 \cdot 10^6 \pm 1.2\%$	$0.70 \cdot 10^5 \pm 0.9\%$

Table 5.1: Total photon flux ( $E\gamma \leq 662$  keV) with statistical error predicted considering a  $^{137}Cs$  activity of 740 GBq at different values of the distance  $D$  to the source along the  $x$ -axis of irradiation field [6].

606 The simulation doesn't directly provides us with an estimated flux at the level  
 607 of our RPC. First of all, it is needed to extract the value of the flux from the  
 608 available data contained in the original paper and then to estimate the flux in 2014  
 609 at the time the experimentation took place. Figure 5.11 that contains the data from

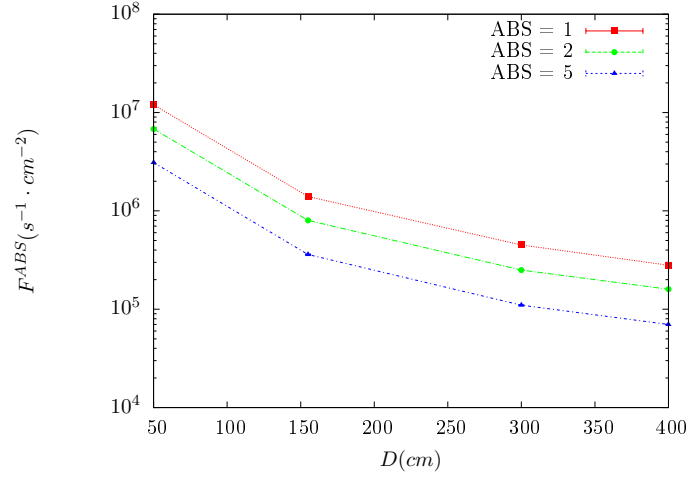


Figure 5.11:  $\gamma$  flux  $F(D)$  is plot using values from table 5.1. As expected, the plot shows similar attenuation behaviours with increasing distance for each absorption factors.

610 Table 5.1. In the case of a pointlike source emitting isotrope and homogeneous  
 611 gamma radiations, the gamma flux  $F$  at a distance  $D$  to the source with respect  
 612 to a reference point situated at  $D_0$  where a known flux  $F_0$  is measured will be  
 613 expressed like in Equation 5.4, assuming that the flux decreases as  $1/D^2$ , where  $c$   
 614 is a fitting factor.

$$F^{ABS} = F_0^{ABS} \times \left( \frac{cD_0}{D} \right)^2 \quad (5.4)$$

615 By rewriting Equation 5.4, it comes that :

$$c = \frac{D}{D_0} \sqrt{\frac{F^{ABS}}{F_0^{ABS}}} \quad (5.5)$$

$$\Delta c = \frac{c}{2} \left( \frac{\Delta F^{ABS}}{F^{ABS}} + \frac{\Delta F_0^{ABS}}{F_0^{ABS}} \right) \quad (5.6)$$

616 Finally, using Equation 5.5 and the data in Table 5.1 with  $D_0 = 50$  cm as  
 617 reference point, we can build Table 5.2. It is interesting to note that  $c$  for each  
 618 value of  $D$  doesn't depend on the absorption factor.

619 For the range of  $D/D_0$  values available, it is possible to use a simple linear  
 620 fit to get the evolution of  $c$ . The linear fit will then use only 2 free parameters,  $a$   
 621 and  $b$ , as written in Equation 5.7. This gives us the results showed in Figure 5.12.  
 622 Figure 5.12b confirms that using only a linear fit to extract  $c$  is enough as the

Nominal ABS	Correction factor $c$		
	at $D = 155$ cm	at $D = 300$ cm	at $D = 400$ cm
1	$1.059 \pm 0.70\%$	$1.162 \pm 0.70\%$	$1.222 \pm 0.70\%$
2	$1.063 \pm 1.10\%$	$1.150 \pm 1.10\%$	$1.227 \pm 0.90\%$
5	$1.056 \pm 1.60\%$	$1.130 \pm 1.60\%$	$1.202 \pm 1.30\%$

Table 5.2: Correction factor  $c$  is computed thanks to formulae 5.5 taking as reference  $D_0 = 50$  cm and the associated flux  $F_0^{ABS}$  for each absorption factor available in table 5.1.

evolution of the rate that can be obtained superimposes well on the simulation points.

$$c\left(\frac{D}{D_0}\right) = a\frac{D}{D_0} + b \quad (5.7)$$

$$F^{ABS} = F_0^{ABS} \left(a + \frac{bD_0}{D}\right)^2 \quad (5.8)$$

$$\Delta F^{ABS} = F^{ABS} \left[ \frac{\Delta F_0^{ABS}}{F_0^{ABS}} + 2 \frac{\Delta a + \Delta b \frac{D_0}{D}}{a + \frac{bD_0}{D}} \right] \quad (5.9)$$

In the case of the 2014 GIF tests, the RPC plane is located at a distance  $D = 206$  cm to the source. Moreover, to estimate the strength of the flux in 2014, it is necessary to consider the nuclear decay through time associated to the Cesium source whose half-life is well known ( $t_{1/2} = (30.05 \pm 0.08)$  y). The very first source activity measurement has been done on the 5<sup>th</sup> of March 1997 while the GIF tests were done in between the 20<sup>th</sup> and the 31<sup>st</sup> of August 2014, i.e. at a time  $t = (17.47 \pm 0.02)$  y resulting in an attenuation of the activity from 740 GBq in 1997 to 494 GBq in 2014. All the needed information to extrapolate the flux through our detector in 2014 has now been assembled, leading to the Table 5.3. It is interesting to note that for a common RPC sensitivity to  $\gamma$  of  $2 \cdot 10^{-3}$ , the order of magnitude of the estimated hit rate per unit area is of the order of the kHz for the fully opened source. Moreover, taking profit of the two working absorbers, it will be possible to scan background rates at 0 Hz,  $\sim 300$  Hz as well as  $\sim 600$  Hz. Without source, a good estimate of the intrinsic performance will be available. Then at 300 Hz, the goal will be to show that the detectors fulfill the performance certification of CMS RPCs. Then a first idea of the performance of the detectors at higher background will be provided with absorption factors 2 ( $\sim 600$  Hz) and 1 (no absorption). *[Here I will also put a reference to the plot showing the estimated background rate at the level of RE3/1 in the case of HL-LHC but this one being in another chapter, I will do it later.]*

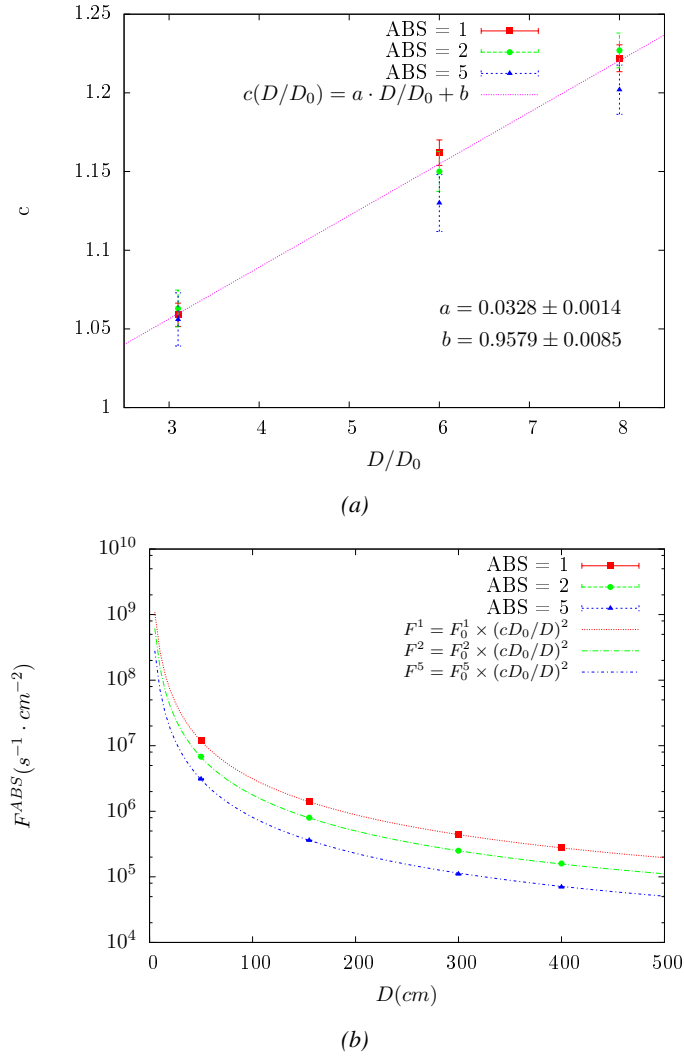


Figure 5.12: Figure 5.12a shows the linear approximation fit done via formulae 5.7 on data from table 5.2. Figure 5.12b shows a comparison of this model with the simulated flux using  $a$  and  $b$  given in figure 5.12a in formulae 5.4 and the reference value  $D_0 = 50cm$  and the associated flux for each absorption factor  $F_0^{ABS}$  from table 5.1



Nominal ABS	Photon flux $F$ [ $s^{-1}cm^{-2}$ ]			Hit rate/unit area [ $Hz\ cm^{-2}$ ] at $D^{2014} = 206\ cm$
	at $D_0^{1997} = 50\ cm$	at $D^{1997} = 206\ cm$	at $D^{2014} = 206\ cm$	
1	$0.12 \cdot 10^8 \pm 0.2\%$	$0.84 \cdot 10^6 \pm 0.3\%$	$0.56 \cdot 10^6 \pm 0.3\%$	$1129 \pm 32$
2	$0.68 \cdot 10^7 \pm 0.3\%$	$0.48 \cdot 10^6 \pm 0.3\%$	$0.32 \cdot 10^6 \pm 0.3\%$	$640 \pm 19$
5	$0.31 \cdot 10^7 \pm 0.4\%$	$0.22 \cdot 10^6 \pm 0.3\%$	$0.15 \cdot 10^6 \pm 0.3\%$	$292 \pm 9$

Table 5.3: The data at  $D_0$  in 1997 is taken from [6]. In a second step, using Equations 5.8 and 5.9, the flux at  $D$  can be estimated in 1997. Then, taking into account the attenuation of the source activity, the flux at  $D$  can be estimated at the time of the tests in GIF in 2014. Finally, assuming a sensitivity of the RPC to  $\gamma\ s = 2 \cdot 10^{-3}$ , an estimation of the hit rate per unit area is obtained.

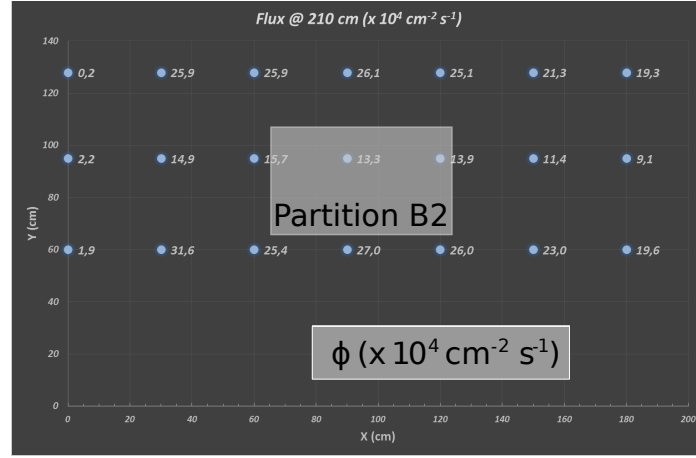


Figure 5.13: Dose measurements has been done in a plane corresponding to the tents front side. This plan is 1900 mm away from the source. As explained in the first chapter, a lens-shaped lead filter provides a uniform photon flux in the vertical plan orthogonal to the beam direction. If the second line of measured fluxes is not taken into account because of lower values due to experimental equipments in the way between the source and the tent, the uniformity of the flux is well showed by the results.

### 5.3 Longevity tests at GIF++

This study implies a monitoring of the performance of the detectors probed using a high intensity muon beam in a irradiated environment by periodically measuring their rate capability, the dark current running through them and the bulk resistivity of the Bakelite composing their electrodes. GIF++, with its very intense  $^{137}Cs$  source, provides the perfect environment to perform such kind of tests. Assuming a maximum acceleration factor of 3, it is expected to accumulate the equivalent charge in 1.7 years.

As the maximum background is found in the endcap, the choice naturally was made to focus the GIF++ longevity studies on endcap chambers. Most of the RPC system was installed in 2007. Nevertheless, the large chambers in the fourth endcap (RE4/2 and RE4/3) have been installed during LS1 in 2014. The Bakelite of these two different productions having different properties, four spare chambers of the present system were selected, two RE2,3/2 spares and two RE4/2 spares. Having two chambers of each type allows to always keep one of them non irradiated as reference, the performance evolution of the irradiated chamber being then compared through time to the performance of the non irradiated one.

The performance of the detectors under different level of irradiation is measured periodically during dedicated test beam periods using the H4 muon beam. In between these test beam periods, the two RE2,3/2 and RE4/2 chambers selected for this study are irradiated by the  $^{137}\text{Cs}$  source in order to accumulate charge and the gamma background is monitored, as well as the currents. The two remaining chambers are kept non-irradiated as reference detectors. Due to the limited gas flow in GIF++, the RE4 chamber remained non-irradiated until end of November 2016 where a new mass flow controller has been installed allowing for bigger volumes of gas to flow in the system.

Figures 5.14 and 5.15 give us for different test beam periods, and thus for increasing integrated charge through time, a comparison of the maximum efficiency, obtained using a sigmoid-like function, and of the working point of both irradiated and non irradiated chambers [7]. No aging is yet to see from this data, the shifts in  $\gamma$  rate per unit area in between irradiated and non irradiated detectors and RE2 and RE4 types being easily explained by a difference of sensitivity due to the various Bakelite resistivities of the HPL electrodes used for the electrode production.

Collecting performance data at each test beam period allows us to extrapolate the maximum efficiency for a background hit rate of  $300 \text{ Hz/cm}^2$  corresponding to the expected HL-LHC conditions. Aging effects could emerge from a loss of efficiency with increasing integrated charge over time, thus Figure 5.16 helps us understand such degradation of the performance of irradiated detectors in comparison with non irradiated ones. The final answer for an eventual loss of efficiency is given in Figure 5.17 by comparing for both irradiated and non irradiated detectors the efficiency sigmoids before and after the longevity study. Moreover, to complete the performance information, the Bakelite resistivity is regularly measured thanks to  $Ag$  scans (Figure 5.18) and the noise rate is monitored weekly during irradiation periods (Figure 5.19). At the end of 2016, no signs of aging were observed and further investigation is needed to get closer to the final integrated charge requirements proposed for the longevity study of the present CMS RPC sub-system.

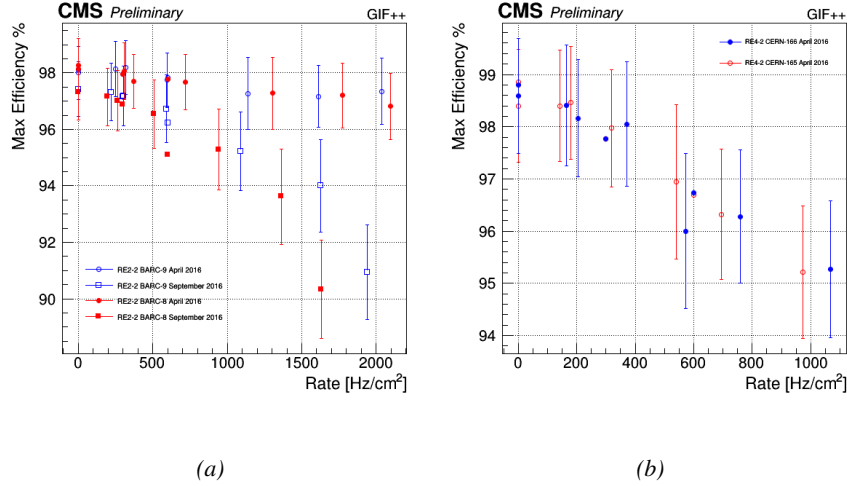


Figure 5.14: Evolution of the maximum efficiency for RE2 (5.14a) and RE4 (5.14b) chambers with increasing extrapolated  $\gamma$  rate per unit area at working point. Both irradiated (blue) and non irradiated (red) chambers are shown.

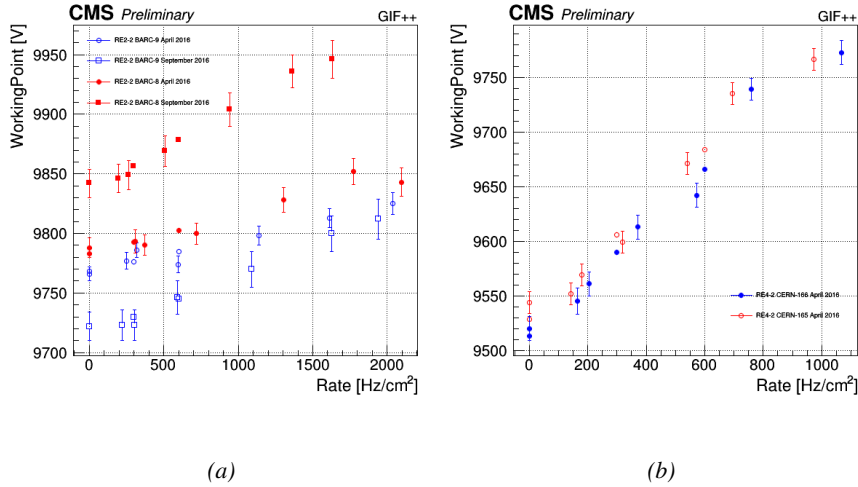


Figure 5.15: Evolution of the working point for RE2 (5.15a) and RE4 (5.15b) with increasing extrapolated  $\gamma$  rate per unit area at working point. Both irradiated (blue) and non irradiated (red) chambers are shown.

### 5.3.1 Description of the Data Acquisition

For the longevity studies, four spare chambers of the present system are used. Two spare RPCs of the RE2,3 stations as well as two spare RPCs from the new

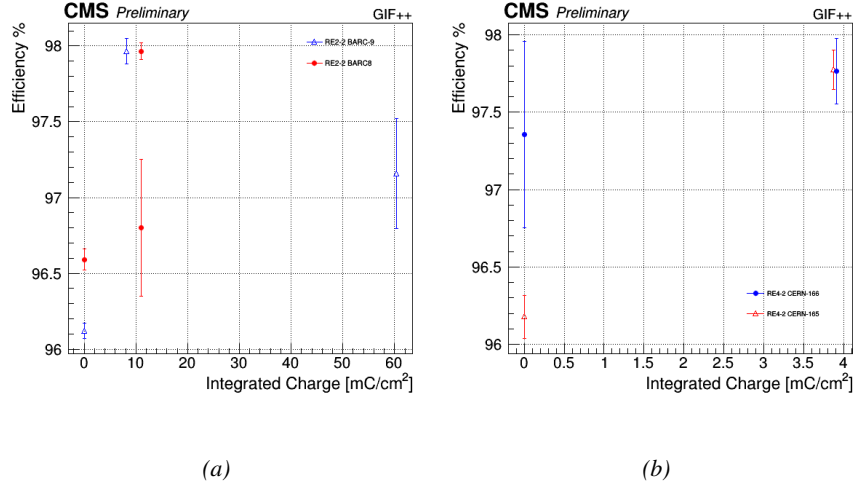


Figure 5.16: Evolution of the maximum efficiency at HL-LHC conditions, i.e. a background hit rate per unit area of  $300 \text{ Hz}/\text{cm}^2$ , with increasing integrated charge for RE2 (5.16a) and RE4 (5.16b) detectors. Both irradiated (blue) and non irradiated (red) chambers are shown. The integrated charge for non irradiated detectors is recorded during test beam periods and stays small with respect to the charge accumulated in irradiated chambers.

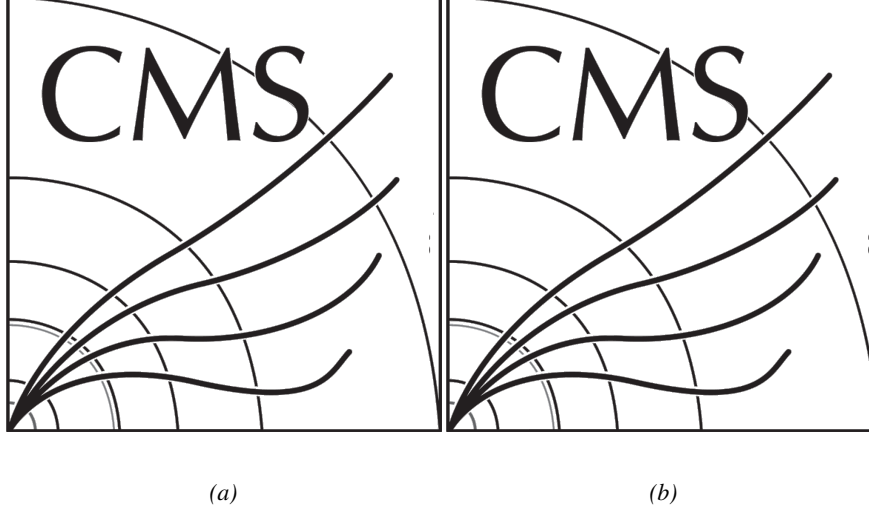


Figure 5.17: Comparison of the efficiency sigmoid before (triangles) and after (circles) irradiation for RE2 (5.17a) and RE4 (5.17b) detectors. Both irradiated (blue) and non irradiated (red) chambers are shown.

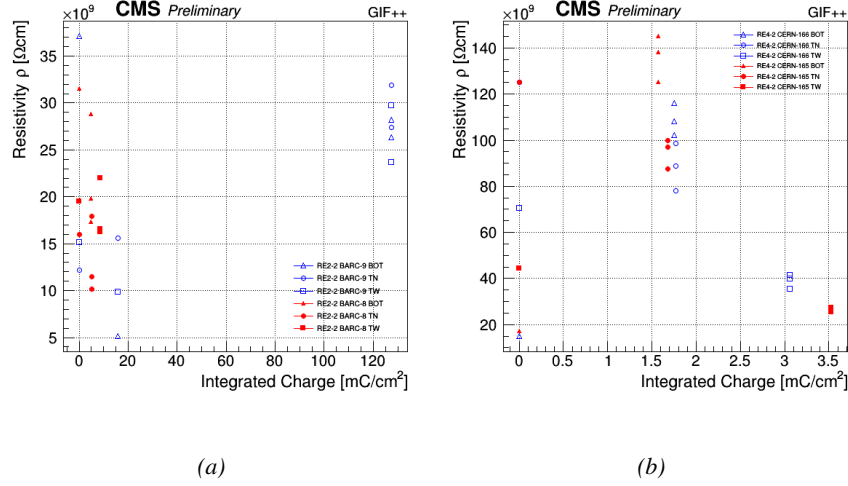


Figure 5.18: Evolution of the Bakelite resistivity for RE2 (5.18a) and RE4 (5.18b) detectors. Both irradiated (blue) and non irradiated (red) chambers are shown.

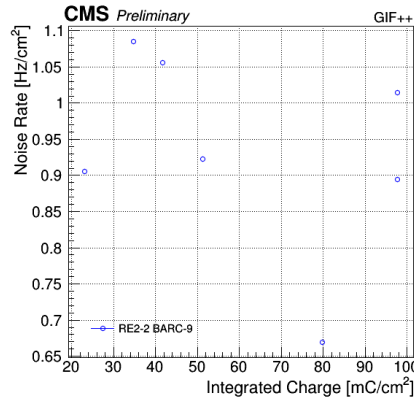


Figure 5.19: Evolution of the noise rate per unit area for the irradiated chamber RE2-2-BARC-9 only.

697 trolley. The trolley is placed inside the GIF++ in the upstream region of the bunker,  
 698 taking the cesium source as a reference. The trolley is oriented for the detection  
 699 surface of the chambers to be orthogonal to the beam line. The system can be  
 700 moved along the orthogonal plane in order to have the beam in all  $\eta$ -partitions.  
 701 For the aging the trolley is moved outside the beam line and is placed in a distance  
 702 of 5.2 m to the source, which irradiates the bunker using an attenuation filter of 2.2  
 703 which corresponds to a fluence of  $10^7 \text{ gamma/cm}^2$ .

During GIF++ operation, the data collected can be divided into different categories as several parameters are monitored in addition to the usual RPC performance data. On one hand, to know the performance of a chamber, it is need to measure its efficiency and to know the background conditions in which it is operated. To do this, the hit signals from the chamber are recorded and stored in a ROOT file via a Data Acquisition (DAQ) software. On the other hand, it is also very important to monitor parameters such as environmental pressure and temperature, gas temperature and humidity, RPC HV, LV, and currents, or even source and beam status. This is done through the GIF++ web Detector Control Software (DCS) that stores this information in a database.

#### 5.3.1.1 GIF++ RPC DAQ

Two different types of tests are conducted on RPCs via the DAQ. Indeed, the performance of the detectors is measured periodically during dedicated test beam periods using the H4 muon beam. In between these test beam periods, when the beam is not available, the chambers are irradiated by the  $^{137}\text{Cs}$  in order to accumulate deposited charge and the gamma background is measured.

RPCs under test are connected through LVDS cables to V1190A Time-to-Digital Converter (TDC) modules manufactured by CAEN. These modules, located in the rack area outside of the bunker, get the logic signals sent by the chambers and save them into their buffers. Due to the limited size of the buffers, the collected data is regularly erased and replaced. A trigger signal is needed for the TDC modules to send the useful data to the DAQ computer via a V1718 CAEN USB communication module.

In the case of performance test, the trigger signal used for data acquisition is generated by the coincidence of three scintillators. A first one is placed upstream outside of the bunker, a second one is placed downstream outside of the bunker, while a third one is placed in front of the trolley, close by the chambers. Every time a trigger is sent to the TDCs, i.e. every time a muon is detected, knowing the time delay in between the trigger and the RPC signals, signals located in the right time window are extracted from the buffers and saved for later analysis. Signals are taken in a time window of 400 ns centered on the muon peak (here we could show a time spectrum). On the other hand, in the case of background rate measurement, the trigger signal needs to be "random" not to measure muons but to look at gamma background. A trigger pulse is continuously generated at a rate of 300 Hz using a dual timer. To integrate an as great as possible time, all signals contained within a time window of 10us prior to the random trigger signal are extracted form the buffers and saved for further analysis (here another time spectrum to illustrate could be useful, maybe even place both spectrum together as a single Figure).

The signals sent to the TDCs correspond to hit collections in the RPCs. When a particle hits a RPC, it induce a signal in the pickup strips of the RPC readout. If this

744 signal is higher than the detection threshold, a LVDS signal is sent to the TDCs.  
 745 The data is then organised into 4 branches keeping track of the event number, the  
 746 hit multiplicity for the whole setup, and the time and channel profile of the hits in  
 747 the TDCs.

#### 748 **5.3.1.2 RPC current, environmental and operation parameter monitoring**

749 In order to take into account the variation of pressure and temperature between  
 750 different data taking periods the applied voltage is corrected following the rela-  
 751 tionship :

$$HV_{eff} = HV_{app} \times \left( 0.2 + 0.8 \cdot \frac{P_0}{P} \times \frac{T}{T_0} \right) \quad (5.10)$$

752 where  $T_0$  (=293 K) and  $P_0$  (=990 mbar) are the reference values.

#### 753 **5.3.2 Tools & Measurements**

754 Insert a short description of the online tools (DAQ, DCS, DQM).  
 755 Insert a short description of the offline tools : tracking and efficiency algorithm.  
 756 Identify long term aging effects we are monitoring the rates per strip.

### 757 **5.4 Results and discussions**

#### 758 **5.4.1 Preliminary studies results**

#### 759 **5.4.2 Longevity studies results**

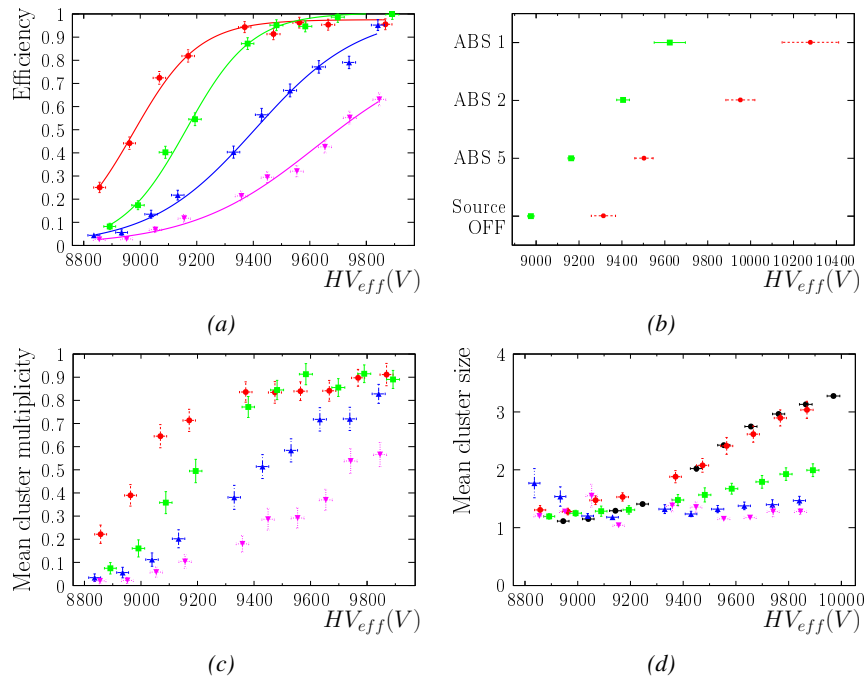


Figure 5.20



# 6

760

761

## Investigation on high rate RPCs

### 762 **6.1 Rate limitations and ageing of RPCs**

#### 763 **6.1.1 Low resistivity electrodes**

#### 764 **6.1.2 Low noise front-end electronics**

### 765 **6.2 Construction of prototypes**

### 766 **6.3 Results and discussions**



# 7

767

768

## Conclusions and outlooks

769 **7.1 Conclusions**

770 **7.2 Outlooks**



## References

- 772 [1] CERN. Geneva. LHC Experiments Committee. *The CMS muon project :  
773 Technical Design Report*. Tech. rep. CERN-LHCC-97-032. CMS Collabora-  
774 tion, 1997.
- 775 [2] CERN. Geneva. LHC Experiments Committee. *Technical Proposal for the  
776 Phase-II Upgrade of the CMS Detector*. Tech. rep. CERN-LHCC-2015-010.  
777 CMS Collaboration, 2015.
- 778 [3] CERN. Geneva. LHC Experiments Committee. *CMS, the Compact Muon  
779 Solenoid : technical proposal*. Tech. rep. CERN-LHCC-94-38. CMS Collab-  
780 oration, 1994.
- 781 [4] M. Abbrescia et al. “Study of long-term performance of CMS RPC under  
782 irradiation at the CERN GIF”. In: *NIMA* 533 (2004), pp. 102–106.
- 783 [5] H.C. Kim et al. “Quantitative aging study with intense irradiation tests for  
784 the CMS forward RPCs”. In: *NIMA* 602 (2009), pp. 771–774.
- 785 [6] S. Agosteo et al. “A facility for the test of large-area muon chambers at high  
786 rates”. In: *NIMA* 452 (2000), pp. 94–104.
- 787 [7] M. Abbrescia et al. “Cosmic ray tests of double-gap resistive plate chambers  
788 for the CMS experiment”. In: *NIMA* 550 (2005), pp. 116–126.





789

790

791

# A data acquisition software for VME CAEN TDCs

792

## **A.1 Introduction**

793

Start text here...







794

795 Details on the online analysis package

796 **B.1 Introduction**

797 insert text here





798

799

800

# Structure of the hybrid simulation software

801

## **C.1 Introduction**

802

insert text here...

